Integrated Systems and Technologies

Cancer Research

Combined PET Imaging of the Inflammatory Tumor Microenvironment Identifies Margins of Unique Radiotracer Uptake

Bastian Zinnhardt[1], Hayet Pigeon[2], Benoit Thézé[2], Thomas Viel[1,3], Lydia Wachsmuth[4], Inga B. Fricke[1], Sonja Schelhaas[1], Lisa Honold[1], Katrin Schwegmann[1], Stefan Wagner[5], Andreas Faust[1], Cornelius Faber[4,6], Michael T. Kuhlmann[1], Sven Hermann[1,6], Michael Schäfers[1,5,6], Alexandra Winkeler[2], and Andreas H. Jacobs[1,6,7]

Abstract

The tumor microenvironment is highly heterogeneous. For gliomas, the tumor-associated inflammatory response is pivotal to support growth and invasion. Factors of glioma growth, inflammation, and invasion, such as the translocator protein (TSPO) and matrix metalloproteinases (MMP), may serve as specific imaging biomarkers of the glioma microenvironment. In this study, noninvasive imaging by PET with [^{18}F]DPA-714 (TSPO) and [^{18}F]BR-351 (MMP) was used for the assessment of localization and quantification of the expression of TSPO and MMP. Imaging was performed in addition to established clinical imaging biomarker of active tumor volume ([^{18}F]FET) in conjunction with MRI. We hypothesized that each imaging biomarker revealed distinct areas of the heterogeneous glioma tissue in a mouse model of human glioma. Tracers were found to be increased 1.4- to 1.7-fold, with [^{18}F]FET showing the biggest volume as depicted by a thresholding-based, volumes of interest analysis. Tumor areas, which could not be detected by a single tracer and/or MRI parameter alone, were measured. Specific compartments of [^{18}F]DPA-714 (14%) and [^{18}F]BR-351 (11%) volumes along the tumor rim could be identified. [^{18}F]DPA-714 (TSPO) and [^{18}F]BR-351 (MMP) matched with histology. Glioma-associated microglia/macrophages (GAM) were identified as TSPO and MMP sources. Multitracer and multimodal molecular imaging approaches may allow us to gain important insights into glioma-associated inflammation (GAM, MMP). Moreover, this noninvasive technique enables characterization of the glioma microenvironment with respect to the disease-driving cellular compartments at the various disease stages. *Cancer Res; 77(8); 1831–41. ©2017 AACR.*

Introduction

Gliomas are highly dynamic, complex, and heterogeneous tissues in which cancer cells themselves stimulate their proliferation, neoangiogenesis, and immune escape to serve their microenvironment (1). In particular, tumor-associated inflammation has been linked to angiogenesis, metastatic potential, and poor prognosis in patients (2). An abundant number of microglia/macrophages are recruited into the tumor, and growing evidence demonstrates that glioma-associated microglia/macrophages (GAM) contribute to glioma growth and invasion, angiogenesis, and immune suppression and represent a pivotal target for therapy (1, 3). In order to better understand the role of glioma-associated inflammation on tumor progression and to follow its impact during treatment, new imaging approaches are crucial to characterize the inflammatory component of the tumor microenvironment. This is even more important in view of new therapeutic approaches for glioma treatment, requiring imaging approaches to allow noninvasive assessment of treatment efficacy and follow-up, as well as detection of a potential therapy-induced switch from a proliferative to an invasive glioma phenotype (4).

Most glioma cells express the 18 kDa translocator protein TSPO. Different studies demonstrated a positive correlation between TSPO expression and grade of malignancy and a negative correlation with survival (5, 6). Within the heterogeneous glioma tissue, different cell types, neoplastic cells, GAMs, and astrocytes also express TSPO (7, 8). Among the current (pre-)clinical PET tracers targeting TSPO, the second-generation tracer, *N,N*-diethyl-2-(2-(4-(2-[^{18}F]fluoroethoxy)phenyl)-5,7-dimethylpyrazolo[1,5-a]pyrimidin-3-yl)acetamide ([^{18}F]DPA-714) has been validated in several models of glioma (7–9) and other neurological diseases (10, 11). Besides being an excellent marker for glioma growth and infiltration, [^{18}F]DPA-714 has shown promise for the detection of GAM activation (8, 12).

[1]European Institute for Molecular Imaging (EIMI), Westfälische Wilhelms-University Münster, Münster, Germany. [2]Imagerie Moléculaire In Vivo, Inserm, CEA, Univ. Paris Sud, CNRS, Université Paris Saclay, CEA - Service Hospitalier Frédéric Joliot, Orsay, France. [3]PARCC INSERM-U970, Université Paris Descartes, Paris, France. [4]Department of Clinical Radiology, University Hospital Münster, Münster, Germany. [5]Department of Nuclear Medicine, University Hospital Münster, Münster, Germany. [6]DFG EXC 1003 Cluster of Excellence `Cells in Motion', University of Münster, Münster, Germany. [7]Department of Geriatrics, Johanniter Hospital, Evangelische Kliniken, Bonn, Germany.

Note: Supplementary data for this article are available at Cancer Research Online (http://cancerres.aacrjournals.org/).

Corresponding Author: Bastian Zinnhardt, University of Münster, Waldeyerstr. 15, Münster, North-Rhine Westphalia 48149, Germany. Phone: 49-251-834-9300; Fax: 49-251-834-9313; E-mail: zinnhardt@wwu.de

doi: 10.1158/0008-5472.CAN-16-2628

Another target for imaging of gliomas are matrix metalloproteinases (MMP). MMPs have been linked to increased cell proliferation, tumor invasion, migration, and poor prognosis in glioma patients (5, 13, 14). Moreover, MMPs facilitate microglia-mediated glioma invasion (15), as for example invasion of glioma cells is reduced in cultured brain slices in the absence of microglia cells (16) or promoted through the increase of MMP-2 expression and activity (17). Besides that MMPs affect the neuroinflammatory milieu by modulating the expression and activity of chemokines, inflammatory cytokines, growth factors, receptor turnover, and by affecting cellular migration (18).

For imaging of activated MMPs, the radiofluorinated MMP inhibitor (*R*)-2-(*N*-benzyl-4-(2-[^{18}F]fluoroethoxy)phenylsulphonamido)-*N*-hydroxy-3-methylbutanamide ([^{18}F]BR-351), a derivative of CGS 25966, has successfully been used for PET imaging of microglia-derived MMPs in a model of ischemic stroke (10). [^{18}F]BR-351 effectively binds to the activated forms of MMP-2, -8, -9, and -13, whereas the latent forms of MMPs are not recognized (19).

Here, we used noninvasive PET imaging of TSPO and MMPs in a mouse model of human orthotopic glioma aiming at detecting specific molecular patterns of glioma pathogenesis *in vivo*. Tumor growth, tumor-associated microglial activation, and MMP activation were studied and related to MRI and PET together with *O*-(2-[^{18}F]fluoroethyl)-*L*-tyrosine ([^{18}F]FET) (20) as the clinical imaging biomarker for assessing glioma extent. The aim of this study was to investigate the combined use of [^{18}F]DPA-714 and [^{18}F]BR-351 as new PET imaging biomarkers of tumor cell signals and the tumor microenvironment. The hypothesis of the study was that each imaging biomarker reveals distinct areas of glioma activity within the heterogeneous glioma tissue.

Materials and Methods

Study design

A multitracer, multimodality approach was used to investigate the feasibility to image TSPO and active MMPs in relation to tumor growth in a mouse model of human glioma.

All experiments were conducted in accordance with the German Law on the Care and Use of Laboratory Animals and approved by the Landesamt für Natur, Umwelt und Verbraucherschutz of North Rhine-Westphalia and the ARRIVE guidelines (https://www.nc3rs.org.uk/arrive-guidelines; ref. 21).

Female NMRI nu/nu mice (Janvier, France), 8 to 11 weeks old, were housed at constant temperature (23°C) and relative humidity (40 %) under a regular light/dark schedule. Food and water were available *ad libitum*.

In total, $n = 27$ mice were orthotopically (intra-striatal injection, coordinates in relation to bregma: lateral −2.0 mm, anterior–posterior +0.5 mm, dorsal–ventral −3.0 mm) implanted with 2×10^5 human Gli36dEGFR-LITG cells in 2 μL PBS. As controls, sham animals ($n = 6$) were injected with 2 μL of PBS only. During anesthesia, body temperature was maintained at physiological level with a custom built heating pad. Mice were imaged 12 to 14 days after orthotopic implantation of glioma cells. First, T2-weighted (T2w) MRI was conducted at day 12 post-implantation, followed by PET acquisition with [^{18}F]DPA-714 on the same day and [^{18}F]BR-351, and [^{18}F]FET on consecutive days (days 13 and 14, respectively; Sequence 1).

A subgroup of mice ($n = 4$) was imaged first with T2w MRI and [^{18}F]FET on the same day, followed by [^{18}F]BR-351 and [^{18}F]DPA-714 on consecutive days (Sequence 2; Supplementary Fig. S1). All imaging experiments were performed within 48 hours.

[^{18}F]DPA-714, [^{18}F]BR-351, and [^{18}F]FET PET, as well as T2w MRI data were available in the same animal. All mice with successful multimodal imaging were included in the data ($n = 20$).

Cell culture

Gli36dEGFR glioma cells were obtained from Dr. David Louis (Molecular Neurooncology Laboratory, Massachusetts General Hospital, Boston, MA; refs. 22, 23). Glioma cells were carefully cultured and observed. Tumor cells displayed typical growth patterns and phenotypes *in vitro* and *in vivo*. The cells were not further genetically authenticated. Cells were cultured as adherent monolayer in DMEM (life Technologies) with high glucose and GlutaMAX (Gibco) supplemented with 10% FBS (Invitrogen), and 1% penicillin/streptomycin (PAA Laboratories) at 37°C in a 5% CO_2/95% air atmosphere.

Radiochemistry

[^{18}F]DPA-714 was prepared following the procedure described in the literature with a radiochemical purity of 99% and a decay corrected radiochemical yield (rcy) of 17.7 ± 8 % (24). The synthesis and quality control of [^{18}F]BR-351 was performed as described previously (19). [^{18}F]BR-351 had a radiochemical purity of 95.5% and a rcy of 7.0 ± 3.4 % due to a small impurity that could not be separated during the last HPLC purification step. [^{18}F]FET was prepared as described previously with a radiochemical purity of 99% and rcy of 23.9 ± 4.3% (25). [^{18}F]DPA-714, [^{18}F]FET, and [^{18}F]BR-351 were formulated in saline/EtOH 17/3 (v/v), water for injection/citrate-puffer/EtOH 19/4/1 (v/v/v) and saline/EtOH 9/1 (v/v), respectively.

PET studies

During all experimental procedures, mice were anesthetized with 1.5% to 2% isoflurane (Abbott Animal Health) in 100% O_2. Mice were subjected to PET imaging using the radiotracers [^{18}F]DPA-714, [^{18}F]BR-351, and [^{18}F]FET for assessment of TSPO expression, MMP activity, and amino acid transport, respectively. PET images were acquired on a high-resolution small animal PET scanner (32 module quadHIDAC, Oxford Positron Systems Ltd.) with uniform spatial resolution (<1 mm FWHM). PET data were reconstructed using one-pass list mode expectation maximization algorithm with resolution recovery (26). [^{18}F]DPA-714 PET images were acquired 45 to 75 minutes post-intravenous injection of 17.7 ± 2.6 MBq [^{18}F]DPA-714. [^{18}F]BR-351 PET images were acquired 95 to 110 minutes post-intravenous injection of 22.4 ± 2.7 MBq [^{18}F]BR-351. [^{18}F]FET PET images were acquired 20 to 30 minutes post-intravenous injection of 10.7 ± 0.7 MBq of [^{18}F]FET (7, 8, 10, 27). After each PET acquisition, the animal bed was transferred into the computed tomography (CT) scanner (Inveon, Siemens Medical Solutions) for anatomic coregistration with the PET images using the image analysis software VINCI (Version: 4.19.0; http://www.nf.mpg.de/vinci3/; refs. 10, 28).

A three step coregistration regimen was applied to assure exact image coregistration. First, PET and CT images were coregistered employing three molecular sieve spheres, (Acros Organics; two on the left side and one at the right side of the animal bed), rinsed in radiotracer solution and taped onto the animal bed, being visible

on CT and PET images. The automated "Landmark tool" was used to superimpose CT images to PET images. The "Magic tool" was further applied to correct for minor mismatches (Step 1, Supplementary Fig. S2). Second, CT images were coregistered to MR images using the "Contour-" and "Fusion-tool" provided by the VINCI software, assisting in delineating the skull and bone of the mice. Several anatomic landmarks were used as quality measures of coregistration: the paraflocculus region (MR) and its respective bone structure (CT), the temporomandibular joint region, the sphenoidal bone, the bulbus olfactorius region, and the lambda region (thickening of the skull dividing the visual cortex from midbrain and cerebellum on top of the inferior colliculus; Step 2, Supplementary Fig. S2). The reslicing parameters of the CT were transferred to the PET, resulting in fused PET-MR images (Step 3, Supplementary Fig. S2). A thorough quality check of image registration in all 3 image planes was performed after PET/CT/MR coregistration. The quality of coregistration was judged and confirmed by three independent experts in the field (B. Zinnhardt, A. Winkeler, and A.H. Jacobs).

MRI studies

MRI was performed with a 9.4 T small animal MR scanner (Bios-Spec 94/20; BrukerBioSpin MRI GmbH). The system was operated using the software ParaVision 5.1. Anatomical 2D T2w rapid acquisition with relaxation enhancement (RARE) brain images were obtained with a helium-cooled Cryoprobe (BrukerBioSpin MRI GmbH) in three imaging planes (TR 3000-5500 ms, TE 50 ms, Rare factor 16, 6 averages, 14–28 contiguous slices, slice thickness 0.5 mm, field of view 20 mm^2, 256 matrix, in plane resolution 78 μm^2, scan time 5–9 minutes, respectively). MRI was conducted for identification of glioma location, and coregistration to PET images.

Data analysis

Image data were analyzed using the in-house developed software MEDgical. Two different volumes of interest (VOI) were defined: (i) an elliptical control VOI covering the striatum (volume 6 mm^3) was drawn on the axial MR images and adjusted on the other imaging planes. This control VOI was reused for every mouse; (ii) a second glioma-covering elliptical VOI (volume 45 mm^3) was drawn in the tumor-affected brain hemisphere, excluding the cerebellum. For quantification, a thresholding approach was applied by multiplying the standard deviation of the control VOI by a factor of 2.5. The resulting counts were added to the mean values of the control region. This was used as minimal threshold level of the affected hemisphere and calculated for all three tracers individually (Supplementary Fig. S3). Tumor-to-background ratios (T/B) were calculated between the glioma VOI (mean and max values) and the contralateral control VOI (mean values). The control VOI constituted a standardized elliptical VOI placed over the left striatum (Supplementary Fig. S3). For volumetric analysis, the resulting volumes of [^{18}F]DPA-714 and [^{18}F]BR-351 were compared with the clinical standard [^{18}F]FET biomarker. First, the combined tracer volumes (union) of [^{18}F]DPA-714 with [^{18}F]FET and [^{18}F]BR-351 with [^{18}F]FET were calculated using the MEDgical software tool. Based on the union of the two tracer volumes the percentage of overlap was calculated. In a next step, the exclusive [^{18}F]DPA-714 and [^{18}F]BR-351 uptake volumes were calculated by subtracting the overlapping volumes of [^{18}F]FET$\cap$[^{18}F]DPA-714 and [^{18}F]FET$\cap$[^{18}F]BR-351 from the total [^{18}F]DPA-714 or [^{18}F]BR-351 signal volume, respectively. The volumetric data were further analyzed comparing the two different sequences of the multitracer approach for assessment of tumor growth effects on volumetry (Supplementary Fig. S4). The intrarater test–retest reproducibility of coregistration was investigated by repeated coregistration on two repeated coregistrations (coreg2 and coreg3) and compared with the initial coregistration procedure (coreg1) in an exemplary set of $n = 6$ mice for the relation of [^{18}F]DPA-714 and [^{18}F]FET (Supplementary Fig. S5).

IHC

After the last imaging examination, mice were sacrificed and perfused with 0.9% NaCl and 4% paraformaldehyde. Brains were fixed and embedded in paraffin. The sections were incubated over night with antibodies for microglia (1:2,000, goat anti-Iba-1, ab107159, Abcam), MMP-9 (1:200, rabbit anti-mouse MMP-9, ab38889, Abcam), and TSPO (1:250, rabbit, anti TSPO, NBP1-95674, Novus Biologicals). Immunohistochemistry for human and murine TSPO was done using the Vector M.O.M. Immunodetection Kit (Vector Laboratories), the specific anti-human TSPO antibody Mab 8D7 (1:500, generously provided by Dr. E. Bribes of Sanofi-Aventis, France; ref. 29) and the specific anti-murine TSPO antibody (1:1,000, generously provided by Dr. M. Higuchi, NIRS, Japan), in 0.5% PBS-TWEEN with 5% BSA for 1 hour at room temperature, followed by incubation with Alexa Fluor 488-conjugated anti-rabbit secondary antibody (1:800, A-21206, Life Technologies), or Alexa Fluor 555 conjugated anti-goat (1:800, A-21432, Life Technologies). Nuclei were stained with DAPI (0.2 μg/mL in PBS, 6335.1, Roth). Conventional histology for TSPO and MMP-9 was performed using biotinylated goat anti-rabbit (1:800, B21078, Life Technologies), followed by HRP–streptavidin incubation (1:600, K1016, DAKO). The staining was visualized by incubation with 3,3-diaminobenzidine (D-5637, Sigma). Images were acquired with a combined fluorescence-light microscope (Nikon Eclipse NI-E, Nikon).

Gel zymography

Mice were transcardially perfused with ice-cold PBS to get rid of excess blood for 2 minutes; brains were immediately harvested afterward. Subsequently, the tumor and the contralateral hemisphere were dissected and snap frozen in liquid nitrogen. The samples were homogenized in a cooled micro dismembrator (Sartorius). Tissue extracts were incubated for 10 minutes in lysis buffer (50 mmol/L TRIS-HCl, 75 mmol/L NaCl, 1 mmol/L phenylmethylsulfonyl fluoride) and centrifuged (4°C, 20 minutes, 1,3000 rpm). An 8% sodium dodecyl sulfate gel containing 0.1% fish skin gelatin (Sigma Aldrich) was prepared. Ten micrograms of total protein were loaded on the gel. Samples were stacked for 20 minutes at 60 V followed by 2 hours at 125 V. The gel was washed in 2.5% Triton-X (30 minutes, room temperature), followed by incubation over night with zymogram developing buffer [50 mmol/L Tris-HCl, 0.2 mol/L NaCl, 5 mmol/L $CaCl_2$, 0.02% Brij 35, in distilled and deionized water (AD)]. The zymogram was stained (1 g Coomassie blue, 90 mL methanol, 20 mL acetic acid, 90 mL AD, 2 hours) and destained (50% methanol, 10% acetic acid, 40% AD, 15 minutes).

In situ zymography

Brains ($n = 2$) were harvested and 15 μm cryosections of the affected brains were sliced. After drying (30 minutes), slices were preincubated with 1× buffer (5 minutes, EnzChek, Life Technologies), and further incubated in a humidified chamber (8 hours,

37°C) with 10× *in situ* zymography reaction buffer (EnzChek), 7× MMP inhibitor (MMPi; cOmplete, Roche), fish skin gelatin (1 mg/mL), and DQ gelatin (EnzChek) in AD. Slices were mounted in DAPI containing mounting medium (Vectashield, H-1500, Vector Laboratories). As controls, slides were additionally incubated with 10 mmol/L of the broad spectrum MMP inhibitor 1,10-phenanthroline (EnzChek) in zymography reaction buffer to block MMP-derived gelatinolytic activity (30).

Statistical analysis

All statistical analyses were performed using Sigma Plot 13.0 software package (Systat Software). All comparisons were tested for normality and variance homogeneity using the Sigma Plot software. Differences in radiotracer uptake ratios between experimental and sham animals were tested using a *t* test, eventually followed by Mann–Whitney *U* test on ranks. The inter-hemispheric difference in the sham group was analyzed using paired *t* tests. Differences in tracer signal volumes and intrarater coreproducibility were tested using a one way repeated measures ANOVA (RM ANOVA), followed by pairwise multiple comparisons using the Holm–Sidak method. Differences between the two groups of different tracer sequences were tested by a one-way ANOVA. Data are shown in Tukey box plots and bar graphs. Significance levels were set at $P < 0.05$.

Results

[^{18}F]DPA-714, [^{18}F]BR-351, and [^{18}F]FET uptake is increased within and around the glioma

Multimodality imaging in a mouse model of glioma for TSPO, MMPs, and amino acid transport revealed increased uptake of all three tracers within and around the tumor as compared with the healthy brain (Fig. 1A). Tumor-to-background (T_{mean}/B_{mean}; Fig. 1C), as well as maximum tumor to mean background (T_{max}/B_{mean}) ratios (Fig. 1D) of all three radiotracers were increased.

[^{18}F]FET signal exceeded the hyperintense tumor area as depicted by T2w MRI. T/B uptake ratios for [^{18}F]FET were also increased compared with sham animals (T_{mean}/B_{mean}: 1.71± 0.21; T_{max}/B_{mean} 2.87 ± 0.65, *t* test, $P < 0.05$ vs. T_{mean}/B_{mean}: 1.09 ± 0.11; T_{max}/B_{mean} 1.57 ± 0.37; Fig. 1). [^{18}F]DPA-714 uptake was located within the tumor and adjacent brain parenchyma. Comparison of [^{18}F]DPA-714 T/B ratios with sham operated animals showed significantly increased uptake (T_{mean}/B_{mean}: 1.82 ± 0.21; T_{max}/B_{mean} 2.98 ± 0.73, t-test, $P < 0.05$ vs. T_{mean}/B_{mean}: 1.11 ± 0.21; T_{max}/B_{mean} 1.91 ± 0.34).

[^{18}F]BR-351 uptake was restricted to the core of the tumor lesion. [^{18}F]BR-351 uptake was increased compared with sham animals (T_{mean}/B_{mean}: 1.83 ± 0.48; T_{max}/B_{mean} 3.19 ± 1.19, *t* test, $P < 0.05$ vs. T_{mean}/B_{mean}: 1.02 ± 0.11; T_{max}/B_{mean}: 2.09 ± 0.65). Within the experimental group, only one animal showed no detectable [^{18}F]BR-351 uptake after application of the thresholding.

For all three tracers, sham operated animals did not show any tracer uptake around the lesion (L) in comparison with the contralateral hemisphere (B) ($L/B_{DPA\text{-}714}$ 1.11 ± 0.21; $L/B_{BR\text{-}351}$ 1.02 ± 0.11; L/B_{FET} 1.09 ± 0.11; Fig. 1B and C).

Volumetric analysis and spatial comparison of tracer volumes

Based on the applied thresholding, the resulting volumes of [^{18}F]DPA-714 and [^{18}F]BR-351 were compared with the clinical standard [^{18}F]FET biomarker, respectively (Fig. 2A).

[^{18}F]FET signal showed the largest mean number of voxel (493.3 ± 134.3; RM ANOVA; $P < 0.05$) compared with [^{18}F]DPA-714 (316.0 ± 105.4) and [^{18}F]BR-351 (179.5 ± 131.5; Fig. 2B).

Comparison of the combination of both tracer volumes (union) of [^{18}F]DPA-714 and [^{18}F]FET uptake volumes showed an overlap of 48.4 ± 11.1% for both tracers.

In order to define volumes of exclusive tracer signal for [^{18}F]DPA-714, the nonoverlapping regions of [^{18}F]DPA-714 were further analyzed by subtracting the overlap of [^{18}F]DPA-714 and [^{18}F]FET from the total [^{18}F]DPA signal. 14 ± 14.5% of the [^{18}F]DPA-714 volumes were nonoverlapping with [^{18}F]FET. 45.1 ± 15.0% of the [^{18}F]FET volumes were nonoverlapping with [^{18}F]DPA-714 (Fig. 2C).

The union of [^{18}F]BR-351 derived signal together with the [^{18}F]FET signal showed an overlap of 28.5 ± 18.0%. Calculation of exclusive [^{18}F]BR-351 signal indicated 11 ± 13.5% of [^{18}F]BR-351 signal as nonoverlapping with [^{18}F]FET, whereas 68.8 ± 21.4% of [^{18}F]FET was nonoverlapping with [^{18}F]BR-351 (Fig. 2D). Areas of exclusive [^{18}F]DPA-714 and [^{18}F]BR-351 were observed at the outer borders of the tumor volume (Fig. 2A). No significant effect on volumetric parameters obtained could be observed when comparing the two different imaging sequences (Supplementary Fig. S4). Exemplary analysis of the volumetric relation of [^{18}F]DPA-714 and [^{18}F]FET to address possible intrarater variability did not reveal significant changes, except for the percentage of [^{18}F]DPA-714 signal for one coregistration (coreg 1 vs. coreg 3: 11.0% ± 3.8 vs. 15.5% ± 5.5; RM ANOVA; $P < 0.05$; Supplementary Fig. S5).

Spatial agreement of radiotracers with histology

Comparison of [^{18}F]DPA-714 and [^{18}F]BR-351 showed spatial agreement of PET volumes with histology for TSPO and *in situ* zymography, respectively (Fig. 3A). Higher magnification images highlight TSPO reactivity arising from tumor cells (Fig. 3C). However, cells of extra-tumoral tissue also displayed TSPO immunoreactivity (Fig. 3C and D). *In situ* zymography signal resulting from gelatinolytic activity revealed MMP activity arising from the tumor tissue (Fig. 3E and F). Sham operated animals display minor TSPO and MMP-9 immunoreactivity along the injection tract (Fig. 3G–K).

Microglia as pivotal TSPO source in glioma

Double immunohistochemistry of TSPO and MMP-9 with Iba-1 (red) indicated infiltrating glioma-GAMs (red) as important source of TSPO and MMP expression, respectively (Fig. 4A). Specific human and murine antibodies against TSPO highlighted human TSPO, hence glioma cells, as important source of TSPO. A fraction of tumor infiltrating cells of murine origin, likely GAMs, also represent a significant source of TSPO (Fig. 4B).

Characterization of MMP activity

In situ zymography depicted gelatinolytic activity (green) arising from tumor cells (blue). Coincubation with the MMP-specific inhibitor 1,10-phenanthroline inhibited gelatinolytic activity within the tumor, suggesting MMP-specific gelatinolytic activity (Fig. 5A). In addition, gel zymography revealed upregulation of MMP-2 and MMP-9 (Fig. 5B).

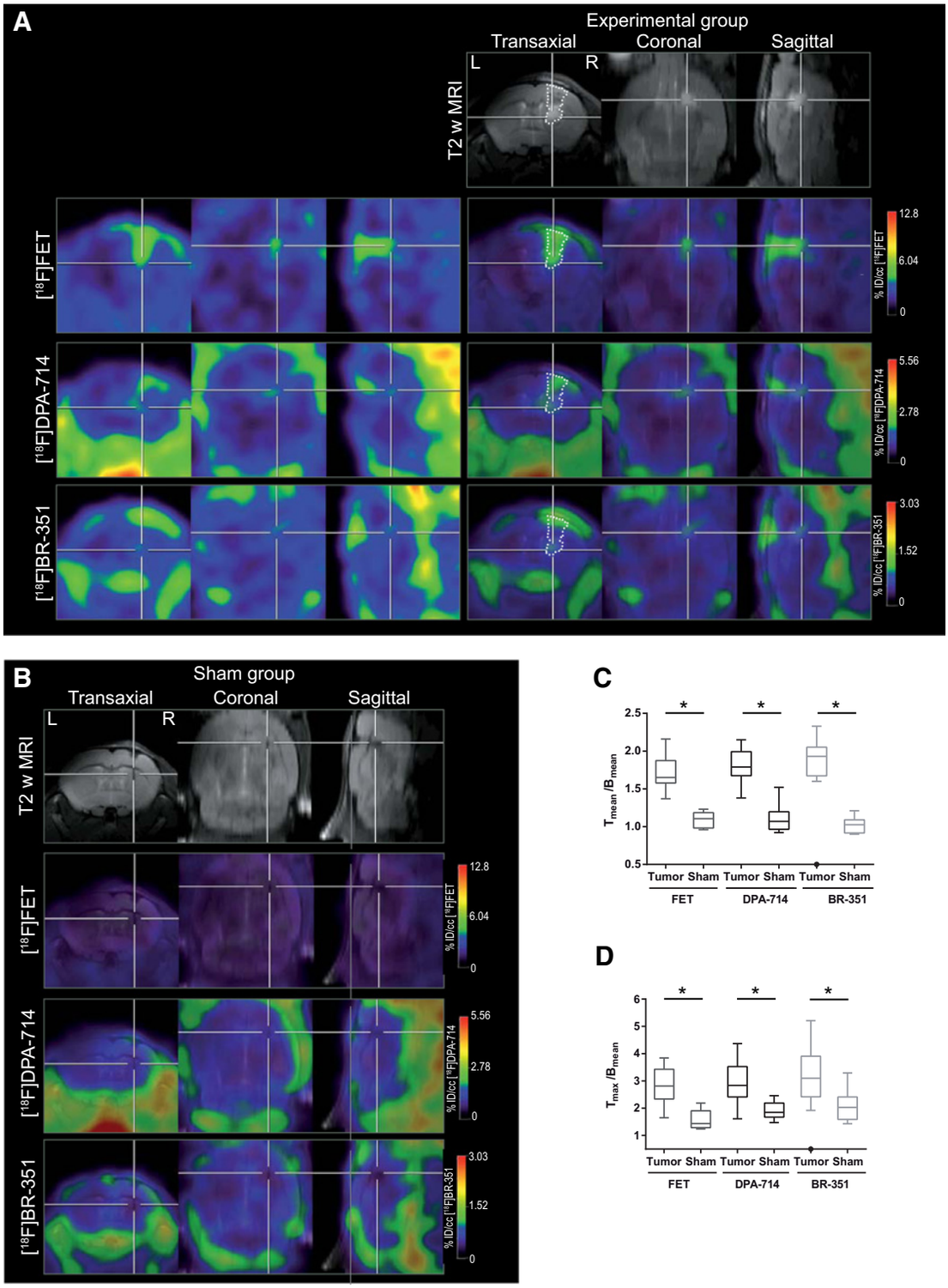

Figure 1.

Multitracer approach to characterize the glioma microenvironment. **A,** PET images for [^{18}F]FET, [^{18}F]DPA-714, and [^{18}F]BR-351 (left, top to bottom) and their fusion with T2w MRI (right, top to bottom). The dotted line indicates the tumor area depicted by MRI and was transferred to PET images. **B,** Representative fusion images of sham-operated animals. **C,** T_{mean}/B_{mean} ratios showed significantly increased uptake for [^{18}F]DPA-714, [^{18}F]BR-351, and [^{18}F]FET. **D,** Investigation of T_{max}/B_{mean} ratios.

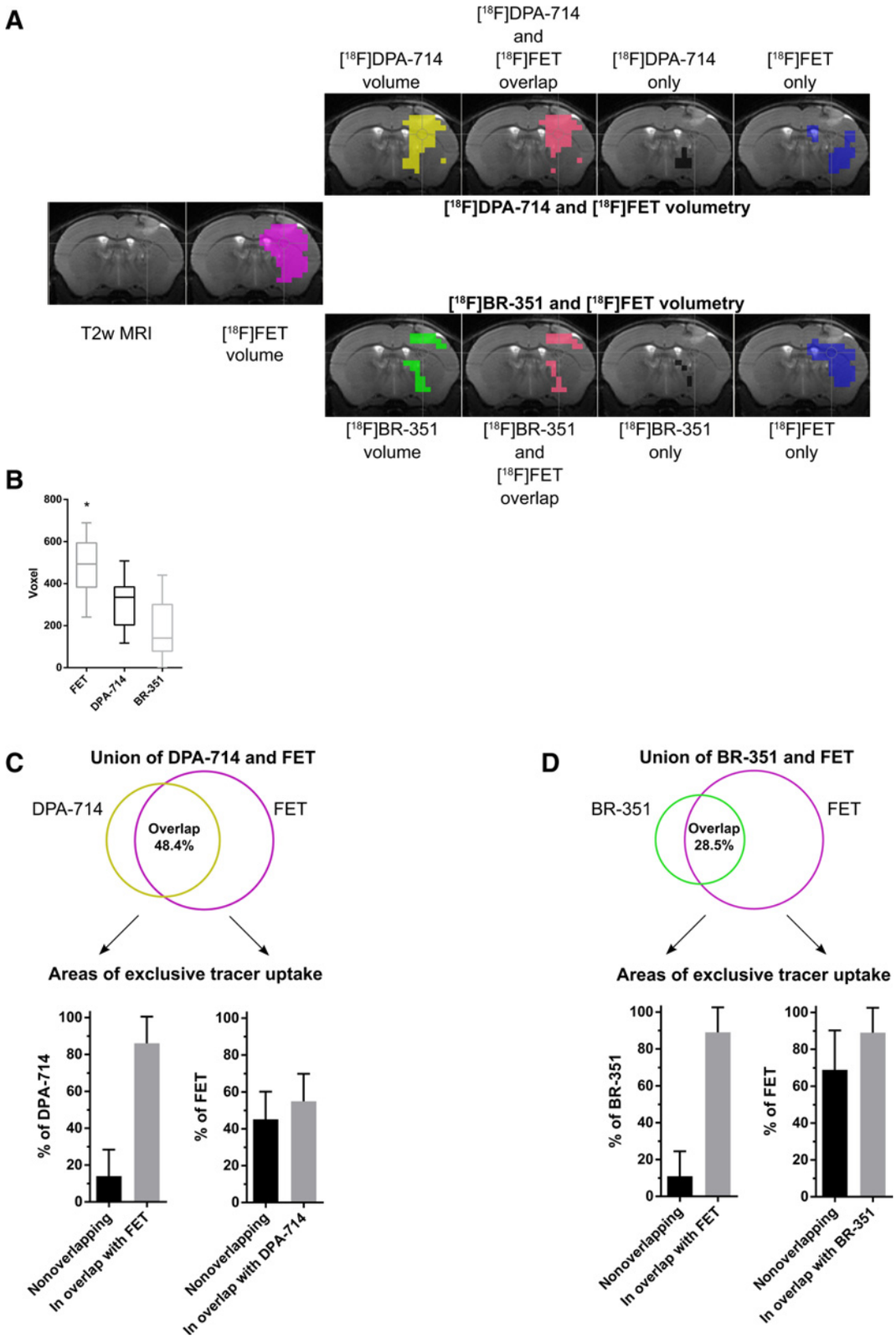

Figure 2.

Volumetric analysis of PET tracer uptake. **A,** Illustration of tracer volumes fused on T2w MRI. **B,** [18F]FET signal volume after thresholding showed the biggest number of voxel, compared with [18F]DPA-714 and [18F]BR-351. **C** and **D,** Comparison of the overlap of the combined tracer volumes, as well as unique areas of tracer uptake.

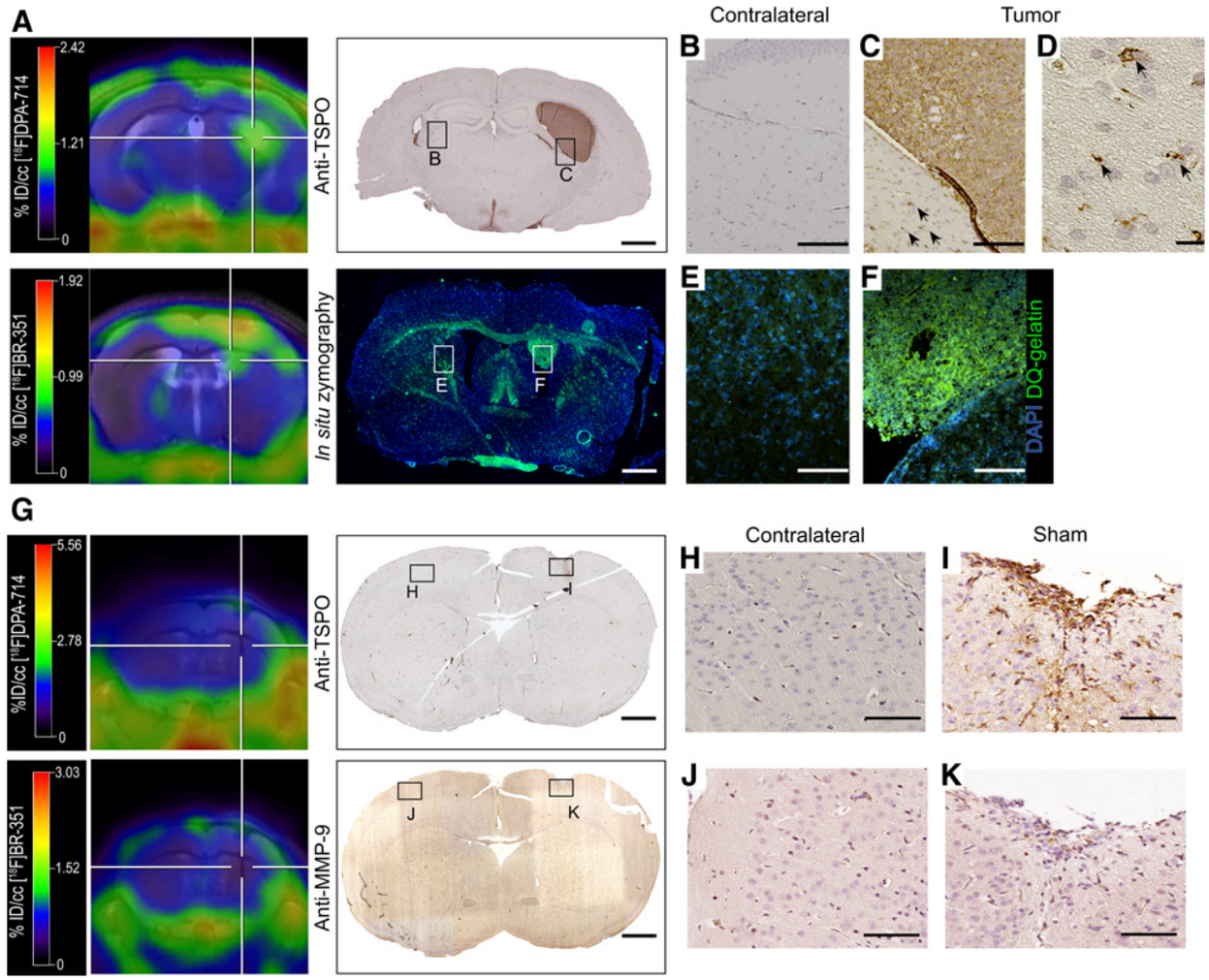

Figure 3.
Spatial comparison of [^{18}F]DPA-714 and [^{18}F]BR-351 with histology and *in situ* zymography. **A,** Comparison of PET data with histology for TSPO and *in situ* zymography revealed good spatial agreement with the respective PET signal. **B–F,** TSPO and MMP signal coming from the tumor cells and surrounding tissue (TSPO, arrows). **G–K,** Sham-operated animals/brains displayed no tracer uptake. Slight immunoreactivity was observed for TSPO along the injection tract (Scale bar, 1,000 μm overview scans; 100/10 μm higher magnification images).

Discussion

This is the first *in vivo* study validating two new radiotracers targeting GAMs (TSPO) and MMP activation in comparison to the clinically established marker for endothelial amino acid transport ([^{18}F]FET) in a murine model of glioma. [^{18}F]DPA-714 uptake was increased in and around the MRI detectable glioma area (∼1.8-fold) mostly related to TSPO-expressing glioma cells. [^{18}F]BR-351 uptake was mostly increased within the core of the tumor to a similar extent as DPA-714 (∼1.8-fold). [^{18}F]FET showed the largest area with increased uptake (∼1.7-fold). Immunohistochemistry and zymography indicated that GAMs may serve as an important source for TSPO and MMP activity. A thresholding approach allowed to depict tumor areas that may not be detected by a single tracer and/or MRI parameter alone. Combining the three radiotracers provides *in vivo* insights into the heterogeneous tissue composition of gliomas with regards to amino acid transport (FET), invasion (BR-351), neoangiogenesis (FET), and inflammation (DPA-714). These biomarkers shall provide the basis for the development of dedicated therapies targeting various tissue compartments within gliomas (e.g., GAMs).

[^{18}F]DPA-714 imaging

Previous studies in glioma bearing rats have highlighted [^{18}F]DPA-714 as a suitable imaging marker for glioma-associated TSPO expression (7–9, 12). In line with these studies, we show, in a murine model of human glioma, a strong increase in [^{18}F]DPA-714 uptake in the tumor region compared with a contralateral region 13 days after implantation of glioma cells. Approximately 50% of the sum of the TSPO signal and the [^{18}F]FET signal overlapped. 14% of [^{18}F]DPA-714 positive glioma

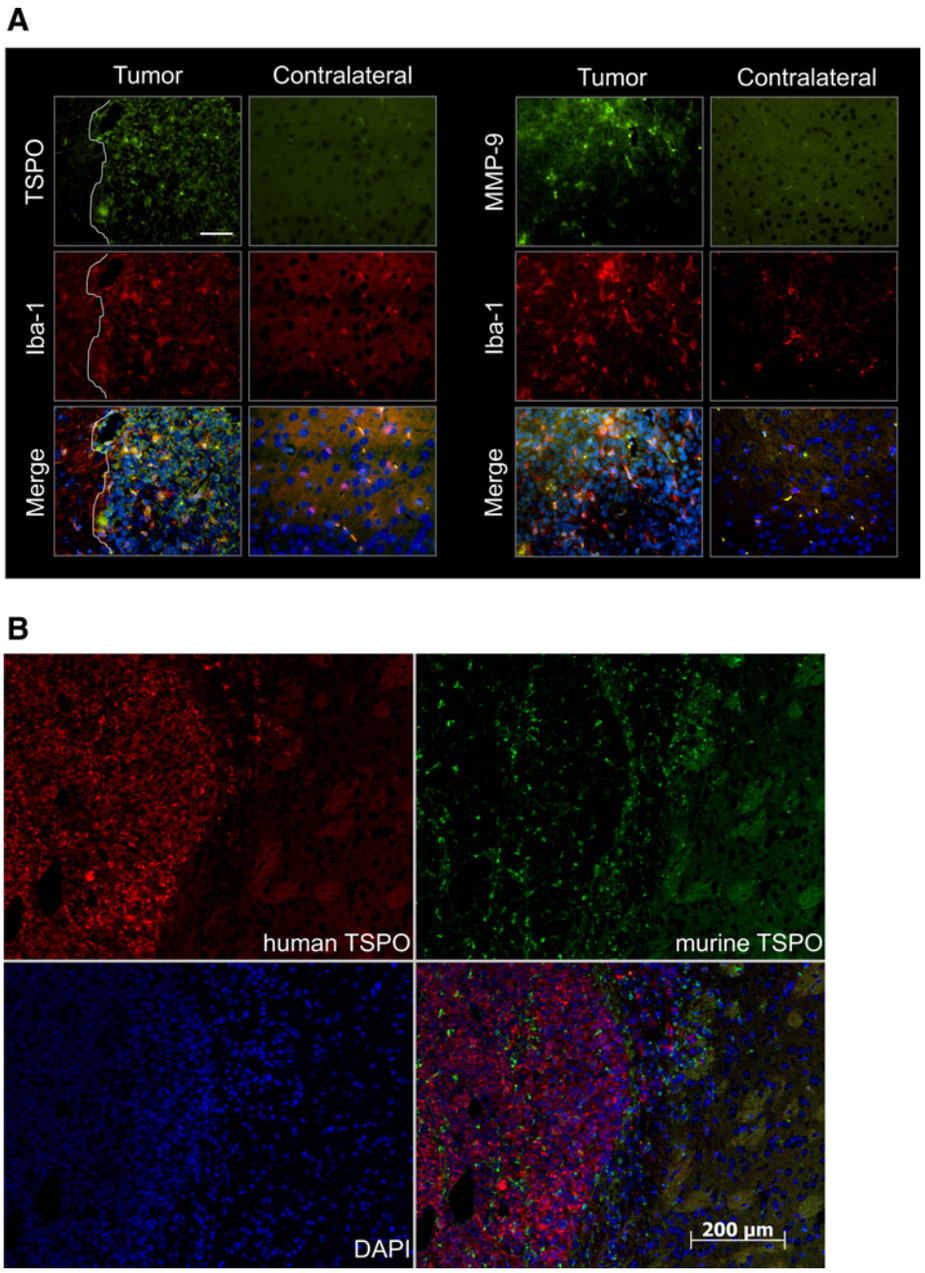

Figure 4.
Role of GAMs for TSPO/MMP signal. **A,** Double immunohistochemistry of Iba-1 (red) with TSPO (green, left) and MMP-9 (green, right) showed Iba-1–expressing cells as source of TSPO and MMP-9. Scale bar, 50 µm. **B,** Comparison of human TSPO (red) and murine TSPO (green) identified tumor cells as major source of TSPO. Infiltrating murine cells also contributed to the TSPO signal. Scale bar, 200 µm.

tissue was exclusive for [^{18}F]DPA-714 and did not reveal [^{18}F]FET uptake, whereas about half of the [^{18}F]FET volumes was not seen by [^{18}F]DPA-714. It should be noted that the tumor growth as well as the intrarater variability may partially have influenced quantitative volumetric numbers. Nevertheless, our observations underline that unique areas of [^{18}F]DPA-714 and [^{18}F]FET are detectable within a comparable range, with no influence by the sequence of image acquisition of the various radiotracers and only minor influence by test–retest variability for the coregistration procedure. Exclusive areas of [^{18}F]DPA-714 uptake in relation to [^{18}F]FET may have been underestimated due to the ongoing tumor growth over the period of image data acquisition.

We specifically chose a sequential imaging approach over a randomized approach potentially reducing bias, as this method yields comparable data with a relatively high sensitivity and relevance with regards to clinical observations (31). In a comparable sequential imaging approach by Jensen and colleagues with GBM patients, the authors combined [^{125}I]CLINDE (TSPO) SPECT followed by [^{18}F]FET and MRI and found similar overlaps of CLINDE and FET (12–42%, $n = 3$), whereas [^{125}I]CLINDE yielded more exclusive areas than [^{18}F]FET compared with MR.

The unique tissue areas at the tumor margins are of high interest, because other research suggested that areas of increased TSPO expression might be related to sites of glioma infiltration

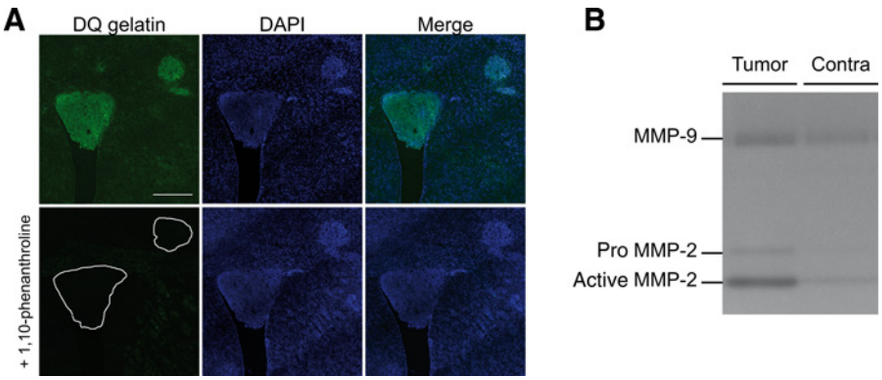

Figure 5.
Determining MMP activity in gliomas. **A,** *In situ* zymography confirmed gelatinolytic activity (green) resulting from the tumor region. Coincubation with 1,10-phenanthroline inhibited gelatinolytic activity. Scale bar, 500 μm. **B,** Gel zymography revealed an increase of activated MMP-2 and MMP-9 in the tumor region compared with the contralateral side.

(12, 31) and the combination of both might improve therapy decisions.

Sham-operated animals displayed mild TSPO expression, which could not be confirmed by [^{18}F]DPA-714 PET, indicative of a TSPO threshold level, as observed previously (10). Correlative histology for TSPO revealed spatial agreement with [^{18}F]DPA-714 radiotracer uptake. Detailed analysis of TSPO sources in conjunction with the marker Iba-1 for microglia/macrophages indicated glioma cells as main source of TSPO expression. In addition, GAMs also contributed to the signal whereas others have shown that normal astrocytes did not seem to play a role (8). Immunohistochemistry with specific antibodies distinguishing human and murine TSPO allowed to depict the different sources of TSPO, indicating that GAMs contributed to the overall [^{18}F]DPA-714 signal. However, it should be noted that the relative contribution of GAMs to glioma TSPO expression may be small (12, 32). Nevertheless GAMs are particularly important, because a significant nonneoplastic part of gliomas consists of infiltrating GAMs (4). They are known to acquire an alternatively activated phenotype and generate an anti-inflammatory, tumor promoting environment, and therefore represent an attractive target for imaging-guided therapy (4). GAM polarization is a highly versatile process *in vivo* (4). Thus, TSPO imaging might be a potential way to monitor GAMs and may help to understand GAM function under normal and treatment conditions.

In line with our data, several studies have shown increased TSPO expression in human glioma biopsies (33–35), experimental glioma (7, 8, 12, 36), but also in GAMs (8). This is of particular importance, because TSPO has been proposed as a marker of glioma invasiveness (37) and elevated levels have been described depending on the tumor grade using *in vivo* imaging (12).

Further research is needed to investigate the suitability of [^{18}F]DPA-714 PET for noninvasive glioma grading and investigation of treatment effects on tumor cells and GAMs. Treatment approaches targeting GAMs in combination with antineoplastic therapies need further attention, because GAMs were shown to be involved in escape from antiangiogenic therapy and represent a potential biomarker for treatment resistance (38).

[^{18}F]BR-351 imaging

MMPs have been shown to be highly upregulated in glioma (39). Accordingly, we show spatial colocalization of [^{18}F]BR-351 with *in situ* zymography, as well as elevated levels of activated MMP-2 and MMP-9 indicated by gel zymography, which are likely the major sources of [^{18}F]BR-351 signal. The elevated expression of the gelatinases, MMP-2, and to a lower extent MMP-9, is indicative of enhanced intracerebral invasion and neoangiogenesis (40). Likewise to [^{18}F]DPA-714, parts of the [^{18}F]BR-351-derived volume were not detected by [^{18}F]FET and thus might hint toward regions of glioma invasion (40). Remarkably, GAMs were found to express MMP-9 on the histologic level. Interestingly, this expression of MMP-9 can be attributed to MMP-2 expressing tumor cells, and is capable of activating infiltrating immune cell derived gelatinases (39). Another link between GAMs and MMPs is the activation of the latent form of MMP-2 through glioma-mediated membrane type-1 MMP expression by microglial cells. This increased expression facilitates glioma invasion (15).

It will be interesting to see whether [^{18}F]BR-351 can be used in other models with enhanced invasiveness and/or neoangiogenesis (41), which are expected to express even higher levels of MMPs to distinguish and characterize different growth patterns *in vivo*.

Besides the gelatinases, [^{18}F]BR-351 can also bind to MMP-13. Although this work did not focus on MMP-13, it should be noted that MMP-13 is also upregulated in glioma. Elevated levels of MMP-13 have been linked to patient survival rates, and are reported as a marker for cancer stem cells (42, 43). Further studies may decipher the potential of [^{18}F]BR-351 in imaging tumor stem cells in glioma.

[^{18}F]FET imaging

[^{18}F]FET is a valuable marker for active tumor volume with significantly higher sensitivity and specificity in diagnosis of brain tumors over, for example, contrast enhanced MRI, [^{18}F]FDG or [^{18}F]FLT PET imaging (20, 44–46). In line with these findings, it has been reported that [^{18}F]FET can be used as prognostic marker of therapy response and it helps to distinguish active tumor volume from therapy-induced tissue alterations or pseudoprogression (47).

However, there is an increasing debate to what extent the glioma-associated inflammatory response affects [^{18}F]FET uptake (48–50). Therefore, a combination of specific tracers targeting the neuroinflammatory response, for example, [^{18}F]DPA-714, with [^{18}F]FET and biopsies may provide a useful tool to depict the relative contribution of inflammation to [^{18}F]FET uptake. We report that [^{18}F]DPA-714 and [^{18}F]FET volumes partially overlap (~50%), which might be an indication that inflammation may be an important contributor to [^{18}F]FET uptake in this model. The overlap may also represent a mixture of cellular compartments (i.e., tumor cells and microglial cells).

In conclusion, multimodal combined PET/MRI has been shown to be superior in delineating active tumor tissue with higher sensitivity and specificity (45, 51). Multitracer and multisequence PET/MRI opens a new avenue for the detailed noninvasive characterization of the heterogeneous glioma tissue with respect to the disease-driving cellular compartments at various disease stages and their response to therapy (vasculature-FET, tumor and inflammatory cells-DPA-714, and proteases-BR-351). Especially, the noninvasive identification of GAMs may represent a fundamental step toward immune cell directed therapies in combination with various targeted or nontargeted antineoplastic agents (4). The detailed characterization of the tumor microenvironment before and after therapy **should** improve the imaging-guided management of patients.

Disclosure of Potential Conflicts of Interest

No potential conflicts of interest were disclosed.

Authors' Contributions

Conception and design: B. Zinnhardt, A.H. Jacobs
Development of methodology: B. Zinnhardt, T. Viel, M.T. Kuhlmann, S. Hermann
Acquisition of data (provided animals, acquired and managed patients, provided facilities, etc.): B. Zinnhardt, H. Pigeon, B. Thézé, L. Wachsmuth, I.B. Fricke, L. Honold, K. Schwegmann, C. Faber, M.T. Kuhlmann
Analysis and interpretation of data (e.g., statistical analysis, biostatistics, computational analysis): B. Zinnhardt, B. Thézé, L. Wachsmuth, S. Schelhaas, L. Honold, C. Faber, S. Hermann, A. Winkeler, A.H. Jacobs
Writing, review, and/or revision of the manuscript: B. Zinnhardt, H. Pigeon, L. Wachsmuth, I.B. Fricke, S. Schelhaas, L. Honold, S. Wagner, A. Faust, C. Faber, M.T. Kuhlmann, S. Hermann, M. Schäfers, A. Winkeler, A.H. Jacobs
Administrative, technical, or material support (i.e., reporting or organizing data, constructing databases): A. Faust
Study supervision: B. Zinnhardt, A.H. Jacobs
Other (establishment and realization of radiotracer production and quality control): S. Wagner
Other (radiotracer production and quality control): A. Faust

Acknowledgments

The authors thank M. Kattenbeck, S. Köster, C. Bätza, R. Priebe, S. Bouma, F. Breuer, I. Hoppe, C. Möllmann, and D. Reinhardt for their excellent technical support, as well as Christian Döring for support on the volumetric analyses.

Grant Support

This research was partly funded by a fellowship of the `Cells-in-Motion' Cluster of Excellence (DFG EXC 1003 - CiM) Graduate School, and the International Max-Planck Research School - Molecular Biomedicine (IMPRS-MBM) Joint Graduate Program' (B. Zinnhardt), the EU 7th Framework Programme (FP7/2007-2013) under grant agreement no. 278850 (INMiND), and by IZKF core unit PIX, Münster, Germany.

The costs of publication of this article were defrayed in part by the payment of page charges. This article must therefore be hereby marked *advertisement* in accordance with 18 U.S.C. Section 1734 solely to indicate this fact.

Received September 30, 2016; revised January 12, 2017; accepted January 12, 2017; published OnlineFirst January 30, 2017.

References

1. Charles NA, Holland EC, Gilbertson R, Glass R, Kettenmann H. The brain tumor microenvironment. Glia 2012;60:502–14.
2. Pierce BL, Ballard-Barbash R, Bernstein L, Baumgartner RN, Neuhouser ML, Wener MH, et al. Elevated biomarkers of inflammation are associated with reduced survival among breast cancer patients. J Clin Oncol 2009;27:3437–44.
3. Richter N, Wendt S, Georgieva PB, Hambardzumyan D, Nolte C, Kettenmann H. Glioma-associated microglia and macrophages/monocytes display distinct electrophysiological properties and do not communicate via gap junctions. Neurosci Lett 2014;583:130–5.
4. Hambardzumyan D, Gutmann DH, Kettenmann H. The role of microglia and macrophages in glioma maintenance and progression. Nat Neurosci 2015;19:20–7.
5. Miettinen H, Kononen J, Haapasalo H, Helén P, Sallinen P, Harjuntausta T, et al. Expression of peripheral-type benzodiazepine receptor and diazepam binding inhibitor in human astrocytomas: relationship to cell proliferation. Cancer Res 1995;55:2691–5.
6. Vlodavsky E, Soustiel JF. Immunohistochemical expression of peripheral benzodiazepine receptors in human astrocytomas and its correlation with grade of malignancy, proliferation, apoptosis and survival. J Neurooncol 2007;81:1–7.
7. Awde AR, Boisgard R, Thézé B, Dubois A, Zheng J, Dollé F, et al. The translocator protein radioligand 18F-DPA-714 monitors antitumor effect of erufosine in a rat 9L intracranial glioma model. J Nucl Med 2013;54:2125–31.
8. Winkeler A, Boisgard R, Awde AR, Dubois A, Thézé B, Zheng J, et al. The translocator protein ligand [18F]DPA-714 images glioma and activated microglia in vivo. Eur J Nucl Med Mol Imaging 2012;39:811–23.
9. Tang D, Hight MR, McKinley ET, Fu A, Buck JR, Smith RA, et al. Quantitative preclinical imaging of TSPO expression in glioma using N,N-diethyl-2-(2-(4-(2-18F-fluoroethoxy)phenyl)-5,7-dimethylpyrazolo[1,5-a]pyrimidin-3-yl)acetamide. J Nucl Med 2012;53:287–94.
10. Zinnhardt B, Viel T, Wachsmuth L, Vrachimis A, Wagner S, Breyholz H-J, et al. Multimodal imaging reveals temporal and spatial microglia and matrix metalloproteinase activity after experimental stroke. J Cereb Blood Flow Metab 2015;35:1711–21.
11. Jacobs AH, Tavitian B, consortium Inm. Noninvasive molecular imaging of neuroinflammation. J Cereb Blood Flow Metab 2012;32:1393–415.
12. Buck JR, McKinley ET, Fu A, Abel TW, Thompson RC, Chambless L, et al. Preclinical TSPO Ligand PET to visualize human glioma xenotransplants: a preliminary study. PLoS ONE 2015;10:e0141659.
13. Lakka SS, Gondi CS, Rao JS. Proteases and glioma angiogenesis. Brain Pathol 2006;15:327–41.
14. Komatsu K, Nakanishi Y, Nemoto N, Hori T, Sawada T, Kobayashi M. Expression and quantitative analysis of matrix metalloproteinase-2 and -9 in human gliomas. Brain Tumor Pathol 2004;21:105–12.
15. Markovic DS, Vinnakota K, Chirasani S, Synowitz M, Raguet H, Stock K, et al. Gliomas induce and exploit microglial MT1-MMP expression for tumor expansion. Proc Natl Acad Sci U S A 2009;106:12530–5.
16. Markovic DS, Glass R, Synowitz M, van Rooijen N, Kettenmann H. Microglia stimulate the invasiveness of glioma cells by increasing the activity of metalloprotease-2. J Neuropathol Exp Neurol 2005;64:754–62.
17. Lin H-C, Song T-Y, Hu M-L. S-Adenosylhomocysteine promotes the invasion of C6 glioma cells via increased secretion of matrix metalloproteinase-2 in murine microglial BV2 cells. Toxicol Sci 2009;112:322–30.
18. McQuibban GA, Gong JH, Wong JP, Wallace JL, Clark-Lewis I, Overall CM. Matrix metalloproteinase processing of monocyte chemoattractant proteins generates CC chemokine receptor antagonists with anti-inflammatory properties in vivo. Blood 2002;100:1160–7.
19. Wagner S, Faust A, Breyholz HJ, Schober O, Schafers M, Kopka K. The MMP inhibitor (R)-2-(N-benzyl-4-(2-[18F]fluoroethoxy)phenylsulphonamido)-N-hydroxy-3-methylbutanamide: Improved precursor synthesis and fully automated radiosynthesis. Appl Radiat Isot 2011;69:862–8.
20. Hutterer M, Nowosielski M, Putzer D, Jansen NL, Seiz M, Schocke M, et al. [18F]-fluoro-ethyl-L-tyrosine PET: a valuable diagnostic tool in neuro-oncology, but not all that glitters is glioma. Neuro Oncol 2013;15:341–51.
21. Kilkenny C, Browne WJ, Cuthill IC, Emerson M, Altman DG. Improving bioscience research reporting: The ARRIVE guidelines for reporting animal research. PLoS Biol 2010;8:e1000412. doi:10.1371/journal.pbio.1000412.
22. Nishikawa R, Ji XD, Harmon RC, Lazar CS, Gill GN, Cavenee WK, et al. A mutant epidermal growth factor receptor common in human glioma

confers enhanced tumorigenicity. Proc Natl Acad Sci U S A 1994;91:7727–31.
23. Abe T, Wakimoto H, Bookstein R, Maneval DC, Chiocca EA, Basilion JP. Intra-arterial delivery of p53-containing adenoviral vector into experimental brain tumors. Cancer Gene Ther 2002;9:228–35.
24. James ML, Fulton RR, Vercoullie J, Henderson DJ, Garreau L, Chalon S, et al. DPA-714, a new translocator protein-specific ligand: synthesis, radiofluorination, and pharmacologic characterization. J Nucl Med 2008;49:814–22.
25. Pauleit D, Stoffels G, Schaden W, Hamacher K, Bauer D, Tellmann L, et al. PET with O-(2-18F-Fluoroethyl)-L-Tyrosine in peripheral tumors: first clinical results. J Nucl Med 2005;46:411–6.
26. Schäfers KP, Reader AJ, Kriens M, Knoess C, Schober O, Schäfers M. Performance evaluation of the 32-module quadHIDAC small-animal PET scanner. J Nucl Med 2005;46:996–1004.
27. Nedergaard MK, Kristoffersen K, Michaelsen SR, Madsen J, Poulsen HS, Stockhausen M-T, et al. The use of longitudinal 18F-FET MicroPET imaging to evaluate response to irinotecan in orthotopic human glioblastoma multiforme xenografts. PLoS ONE 2014;9:e100009.
28. Vollmar SCJ, Sue M, Klein J, Jacobs AH, Herholz K. VINCI-Volume Imaging in Neurological Research, Co-Registration and ROIs Forschung und wissenschaftliches Rechnen 2003. Göttingen Gesellschaft für wissenschaftliche Datenverarbeitung 2004;115–31.
29. Bribes E, Carrière D, Goubet C, Galiègue S, Casellas P, Simony-Lafontaine J. Immunohistochemical assessment of the peripheral benzodiazepine receptor in human tissues. J Histochem Cytochem 2004;52:19–28.
30. Bremer C, Tung C-H, Weissleder R. In vivo molecular target assessment of matrix metalloproteinase inhibition. Nat Med 2001;7:743–8.
31. Jensen P, Feng L, Law I, Svarer C, Knudsen GM, Mikkelsen JD, et al. TSPO imaging in glioblastoma multiforme: a direct comparison between 123I-CLINDE SPECT, 18F-FET PET, and gadolinium-enhanced MR imaging. J Nucl Med 2015;56:1386–90.
32. Janczar K, Su Z, Raccagni I, Anfosso A, Kelly C, Durrenberger PF, et al. The 18-kDa mitochondrial translocator protein in gliomas: from the bench to bedside. Biochem Soc Trans 2015;43:579–85.
33. Black KL, Ikezaki K, Santori E, Becker DP, Vinters H V. Specific high-affinity binding of peripheral benzodiazepine receptor ligands to brain tumors in rat and man. Cancer 1990;65:93–7.
34. Junck L, Olson JM, Ciliax BJ, Koeppe RA, Watkins GL, Jewett DM, et al. PET imaging of human gliomas with ligands for the peripheral benzodiazepine binding site. Ann Neurol 1989;26:752–8.
35. Olson JM, Junck L, Young AB, Penney JB, Mancini WR. Isoquinoline and peripheral-type benzodiazepine binding in gliomas: implications for diagnostic imaging. Cancer Res 1988;48:5837–41.
36. Buck JR, McKinley ET, Hight MR, Fu A, Tang D, Smith RA, et al. Quantitative, preclinical PET of translocator protein expression in glioma using 18F-N-fluoroacetyl-N-(2,5-dimethoxybenzyl)-2-phenoxyaniline. J Nucl Med 2011;52:107–14.
37. Veenman L, Levin E, Weisinger G, Leschiner S, Spanier I, Snyder SH, et al. Peripheral-type benzodiazepine receptor density and in vitro tumorigenicity of glioma cell lines. Biochem Pharmacol 2004;68:689–98.
38. Lu-Emerson C, Snuderl M, Kirkpatrick ND, Goveia J, Davidson C, Huang Y, et al. Increase in tumor-associated macrophages after antiangiogenic therapy is associated with poor survival among patients with recurrent glioblastoma. Neuro Oncol 2013;15:1079–87.
39. Koutroulis I, Zarros A, Theocharis S. The role of matrix metalloproteinases in the pathophysiology and progression of human nervous system malignancies: a chance for the development of targeted therapeutic approaches? Expert Opin Ther Targets 2008;12:1577–86.
40. Forsyth PA, Laing TD, Gibson AW, Rewcastle NB, Brasher P, Sutherland G, et al. High levels of gelatinase-B and active gelatinase-A in metastatic glioblastoma. J Neurooncol 1998;36:21–9.
41. Viel T, Schelhaas S, Wagner S, Wachsmuth L, Schwegmann K, Kuhlmann M, et al. Early assessment of the efficacy of temozolomide chemotherapy in experimental glioblastoma using [18F]FLT-PET imaging. PLoS ONE 2013;8:e67911.
42. Inoue A, Takahashi H, Harada H, Kohno S, Ohue S, Kobayashi K, et al. Cancer stem-like cells of glioblastoma characteristically express MMP-13 and display highly invasive activity. Int J Oncol 2010;37:1121–31.
43. Okoye-Okafor UC, Bartholdy B, Cartier J, Gao EN, Pietrak B, Rendina AR, et al. New IDH1 mutant inhibitors for treatment of acute myeloid leukemia. Nat Chem Biol 2015;11:878–86.
44. Pauleit D, Floeth F, Hamacher K, Riemenschneider MJ, Reifenberger G, Müller H-W, et al. O-(2-[18F]fluoroethyl)-L-tyrosine PET combined with MRI improves the diagnostic assessment of cerebral gliomas. Brain 2005;128:678–87.
45. Nowosielski M, Difranco MD, Putzer D, Seiz M, Recheis W, Jacobs AH, et al. An intra-individual comparison of MRI, [18F]-FET and [18F]-FLT PET in patients with high-grade gliomas. PLoS ONE 2014;9:e95830.
46. Galldiks N, Langen K-J, Holy R, Pinkawa M, Stoffels G, Nolte KW, et al. Assessment of treatment response in patients with glioblastoma using O-(2-18F-fluoroethyl)-L-tyrosine PET in comparison to MRI. J Nucl Med 2012;53:1048–57.
47. Hutterer M, Nowosielski M, Putzer D, Waitz D, Tinkhauser G, Kostron H, et al. O-(2-18F-fluoroethyl)-L-tyrosine PET predicts failure of antiangiogenic treatment in patients with recurrent high-grade glioma. J Nucl Med 2011;52:856–64.
48. Hutterer M, Nowosielski M, Putzer D, la Fougère C, Virgolini IJ, Jacobs AH, et al. Response to "reply to [18F]-fluoro-ethyl-L-tyrosine PET: a valuable diagnostic tool in neuro-oncology, but not all that glitters is glioma" by Hutterer et al. Neuro Oncol 2013;15:814–5.
49. Langen K-J, Galldiks N. Reply to "[18F]-fluoro-ethyl-L-tyrosine PET: a valuable diagnostic tool in neuro-oncology, but not all that glitters is glioma" by Hutterer et al. Neuro Oncol 2013;15:816–7.
50. Piroth MD, Prasath J, Willuweit A, Stoffels G, Sellhaus B, van Osterhout A, et al. Uptake of O-(2-[18F]fluoroethyl)-L-tyrosine in reactive astrocytosis in the vicinity of cerebral gliomas. Nucl Med Biol 2013;40:795–800.
51. Dhermain FG, Hau P, Lanfermann H, Jacobs AH, van den Bent MJ. Advanced MRI and PET imaging for assessment of treatment response in patients with gliomas. Lancet Neurol 2010;9:906–20.